Article

Hollow Mesoporous CeO$_2$-Based Nanoenzymes Fabrication for Effective Synergistic Eradication of Malignant Breast Cancer via Photothermal–Chemodynamic Therapy

Huaxin Tan [1], Yongzhen Li [1], Jiaying Ma [1], Peiyuan Wang [2,3], Qiaoling Chen [2,*] and Lidan Hu [1,*]

[1] Department of Biochemistry and Molecular Biology, The Key Laboratory of Ecological Environment and Critical Human Diseases Prevention of Hunan Province Department of Education, School of Basic Medicine, Hengyang Medical School, University of South China, Hengyang 421001, China
[2] Department of Anesthesiology, The First Affiliated Hospital of Xiamen University, Xiamen 361001, China
[3] Key Laboratory of Design and Assembly of Functional Nanostructures, Fujian Institute of Research on the Structure of Matter, Chinese Academy of Sciences, Fuzhou 350002, China
[*] Correspondence: mz1262585085@outlook.com (Q.C.); hulidan@usc.edu.cn (L.H.)

Abstract: CeO$_2$-based nanoenzymes present a very promising paradigm in cancerous therapy, as H$_2$O$_2$ can be effectively decomposed under the electron transmit between Ce^{3+} and Ce^{4+}. However, the limitations of endogenous H$_2$O$_2$ and intracellular low Fenton-like reaction rate lead to single unsatisfied chemodynamic therapy (CDT) efficacy. Other therapeutic modalities combined with chemodynamic therapy are generally used to enhance the tumor eradiation efficacy. Here, we have synthesized a novel hollow pH-sensitive CeO$_2$ nanoenzyme after a cavity is loaded with indocyanine green (ICG), as well as with surface modification of tumor targeting peptides, Arg-Gly-Asp (denoted as HCeO$_2$@ICG-RGD), to successfully target tumor cells via $\alpha_v\beta_3$ recognition. Importantly, in comparison with single chemodynamic therapy, a large amount of reactive oxygen species in cytoplasm were induced by enhanced chemodynamic therapy with photothermal therapy (PTT). Furthermore, tumor cells were efficiently killed by a combination of photothermal and chemodynamic therapy, revealing that synergistic therapy was successfully constructed. This is mainly due to the precise delivery of ICG and release after HCeO$_2$ decomposition in cytoplasm, in which effective hyperthermia generation was found under 808 nm laser irradiation. Meanwhile, our HCeO2@ICG-RGD can act as a fluorescent imaging contrast agent for an evaluation of tumor tissue targeting capability in vivo. Finally, we found that almost all tumors in HCeO$_2$@ICG-RGD+laser groups were completely eradicated in breast cancer bearing mice, further proving the effective synergistic effect in vivo. Therefore, our novel CeO$_2$-based PTT agents provide a proof-of-concept argumentation of tumor-precise multi-mode therapies in preclinical applications.

Keywords: hollow CeO$_2$-based nanoenzyme; ICG; chemodynamic therapy enhancement; photothermal therapy; synergistic effect

1. Introduction

Similar to toxic substances, reactive oxygen species (ROS) can induce tumor cell apoptosis by destroying biological molecules, such as functional protein or DNA damage [1–3]. Chemodynamic therapy (CDT), as the most well-known ROS-based anticancer strategy, has attracted widespread attention. Compared with some oxygen-dependent therapeutic modalities, such as photodynamic therapy (PDT) under laser irradiation or sonodynamic therapy with untrasound-assistance [4–6], CDT could exert a significant antitumor capability under the hypoxia tumor microenvironment without any other external facilities [7]. Frequently, CDT employs catalysts, such as metal-based nanomaterials to initiate Fenton-like reactions, which are capable of converting intracellular hydrogen peroxide (H$_2$O$_2$) into

toxic oxidative hydroxyl radicals (•OH). Consequently, this leads to tumor cell apoptosis [8]. In addition, CDT ensures normal cell safety by suppressing Fenton-like reactions with insufficient H_2O_2 under normal physiological microenvironment [9]. In recent years, nanoenzymes as nanocatalytic therapeutics, have been extensively used for antitumor applications, owing to their parallel catalytic activity toward natural enzymes and unique properties [10–12]. Numerous nanomaterials have been explored as nanoenzymes with various sizes and functional groups on the surface, which showed predominant potential in tumor eradication [13–17]. Among these nanoenzymes, cerium oxide (CeO_2) nanomaterials can be applied as candidates for the development of tumor therapeutic nanoplatforms due to their catalase and peroxidase activity toward high H_2O_2 in tumor microenvironment at various pH values [18]. Interestingly, several studies recently discovered that H_2O_2 can absorb onto the surface of CeO_2 nanocatalyst, in which a stable CeO_2–H_2O_2 complex can be formed [19,20]. Specifically, under acidic microenvironment, the coordinated H_2O_2 molecules undergo a disproportionation procedure to yield two hydroxyl radical generation rates with overwhelming cytotoxicity against cancerous cells. Moreover, this process can be regarded as CDT [9,21–23]. Accordingly, CeO_2-based nanoparticles are the rational choice in the construction of CDT-based tumor therapeutic nanoplatforms. However, to date, owing to the restriction from the total amount of H_2O_2 in cytoplasm of tumor cells, CDT is still not able to obtain satisfactory therapeutic performance. Therefore, improving the efficacy of CDT is the main challenge during the clinical translation of CDT nanoplatforms.

To improve the tumor therapeutic effect of CDT, combining other therapies to achieve the synergistic therapy is a relatively ideal choice. Generally, CDT nanoplatforms are designed based on metal oxide nanoparticles. This design is very convenient for loading or anchoring other therapeutics to achieve combination therapy. Similar to anticancer drugs, camptothecin can be successfully loaded into Fe-based metal organic frameworks (MOF) to combine CDT with chemotherapy [24]. Specifically, indocyanine green (ICG) has been reported to be an effective NIR light absorber for laser-mediated photothermal therapy, that has been approved by the Food and Drug Administration (FDA) [25–27]. Ce doped Cu–Al layered double hydroxide ultrathin nanosheets with indocyanine-green (ICG)-loaded nanoparticles were capable of generating effective hyperthermia, which substantially heightens the Fenton-like reaction of Cu^+ and Ce^{3+} with local H_2O_2 [28]. Interestingly, an increased local tumor temperature induced by PTT could result in the generation of hydroxyl radicals. Meanwhile, the production of a large amount of toxic hydroxyl radicals further delays the heat shock protein expression, which leads the cancerous cells to be more sensitive toward heat [29–33]. Therefore, the synergistic enhancement of PTT+CDT in tumor therapy could be achieved. In this context, the co-delivery of ICG nanosystem through the CeO_2 nanoenzyme is expected to achieve specific and enhanced therapeutic effects.

Based on the above investigations, we herein demonstrate the successful fabrication of a novel hollow CeO_2 nanoenzyme with ICG loading ($HCeO_2$@ICG). This can serve as the active therapeutic nanoenzyme for CDT via Ce^{3+}/Ce^{4+} under acidic microenvironment and Fenton-like reation ehancement by PTT, as illustrated in Figure 1. After modification of NH_2 groups on the surface of tumor cell membrane $\alpha_v\beta_3$ targted peptides, RGD molecules were successfully anchored on the surface of $HCeO_2$@ICG ($HCeO_2$@ICG-RGD). This nanoenzyme could be effectively targeted in tumor tissues and degraded in lysosome for ICG release. Furthermore, the degraded CeO_2 can be used for ROS generation. Importantly, hyperthermia generated under 808 nm laser irradiation further facailited intracellular ROS production. After tail vein injection, $HCeO_2$@ICG-RGD can be used as a contrasting agent in the second near-infrared region window (NIR II, 900–1700 nm). It accumulates in solid tumor at 24 h post-injection, under the observation of NIR II fluorescent imaging, then after 808 nm laser irradiation for 5 min, malignant tumors were completely eradicated. These findings demonstrate the great potential of ICG-loaded CeO_2-based hollow nanoenzyme for clinical translation of malignant breast cancer inhibition.
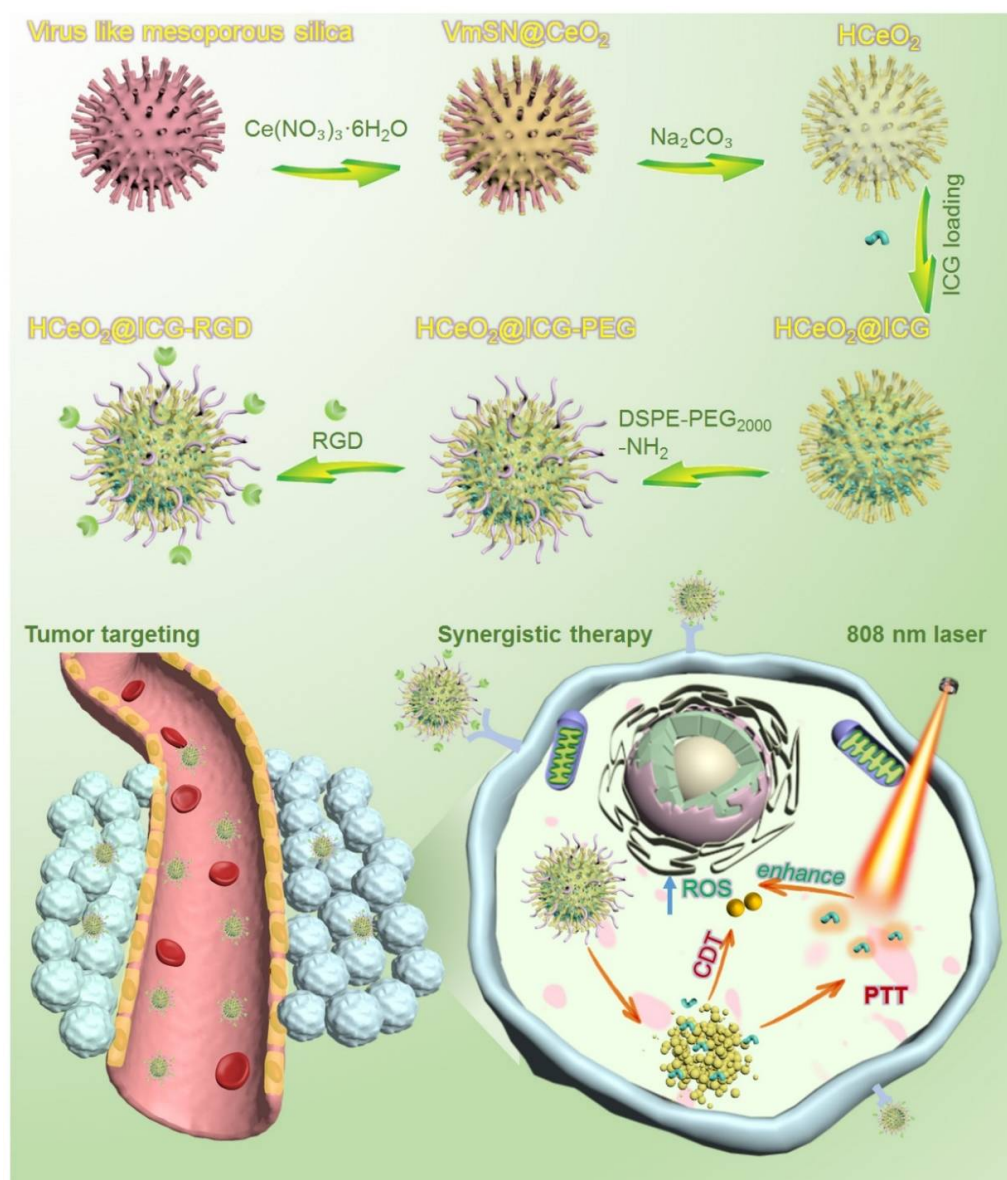
Figure 1. Schematic illustration of stepwise $HCeO_2$@ICG-RGD fabrication for precise synergistic eradication of malignant tumors via PTT enhanced CDT.

2. Materials and Methods

2.1. Virus-like Mesoporous Silica Synthesis

The virus-like mesoporous silica template was obtained by a special epitaxial growth approach with the hexadecyltrimethylammonium (CTAB) as the template, tetraethyl orthosilicate (TEOS) as a Si precursor, NaOH as the reductant, and cyclohexane as the oil solvent [34]. Typically, 1.0 g of CTAB and 0.8 mL of NaOH (0.1 M) were first added to 50 mL of H_2O_2 and stirred in oil bath at 60 °C for 30 min. Then, 20 mL of 20% of TEOS/cyclohexane mixture was added to the water layer and stirring was maintained in oil bath at 60 °C for 2 days. Thereafter, the as-made products were alternatively washed 6 times by water and ethanol, followed by centrifugation at 13,000 rpm for 10 min. Finally, the virus-like mesoporous nanoparticles were dispersed in 50 mL of acetone and refluxed at 60 °C in oil bath for more than 12 h to remove the residual surfactants. The final silica samples were alternatively washed by water and ethanol, followed by drying under vacuum overnight at 45 °C.

2.2. HCeO₂@ICG Synthesis

For HCeO$_2$@ICG synthesis, 100 mg of virus-like silica templates and Ce(NO$_3$)$_3$·6H$_2$O (0.1232 g) were first co-dissolved in 50 mL of deionized water and moderately stirred for 30 min at 90 °C in oil bath. Then, 0.105 g of hexamethylenetetramine power was added to this mixture, and the solution was vigorously stirred for 120 min at 90 °C in oil bath. The final core-shell samples (VmSi@CeO$_2$) were washed three times by deionized water, followed by centrifugation at 5000 rpm for 5 min and oven dried for 12 h at 60 °C. Finally, the hard template, virus-like mesoporous silica was etched using 60 mL of 0.1 M Na$_2$CO$_3$, stirred at 75 °C in oil bath for 12 h, and washed more than three times with deionized water. After oven-drying (60 °C) the mixture overnight, hollow mesoporous cerium oxide nanoparticles with rough surface (HCeO$_2$) were obtained.

Furthermore, 1 mg of ICG was dissolved in ethanol (2.0 mL). Then, 25 mg of HCeO$_2$ was added to the above mixture and the solution was continuously stirred for 48 h under room temperature. The ICG molecules could be successfully adsorbed onto the stacking mesopores and the hollow cavity of HCeO$_2$. The as-made ICG-loaded HCeO$_2$ nanoenzymes (HCeO$_2$@ICG) were washed three times, followed by by centrifugation at 5000 rpm for 10 min. The precise loading of ICG content in HCeO$_2$@ICG was quantified from a standard curve by measuring the UV absorbance.

2.3. HCeO₂@ICG-RGD Synthesis

For HCeO$_2$@ICG-RGD synthesis, 100 mg of HCeO$_2$@ICG and 20 mg of DSPE-PEG$_{2000}$-NH$_2$ were first co-dissolved in 5 mL of chloroform. Then, the amino group modified HCeO$_2$@ICG (HCeO$_2$@ICG-PEG) was obtained after the chloroform was all slowly evaporated in a fume cupboard. After the removal of residual DSPE-PEG$_{2000}$-NH$_2$ by ultra-centrifugation at 15,000 rpm for 30 min, the as-made HCeO$_2$@ICG-PEG was acquired and re-dispersed in deionized water.

Subsequently, HCeO$_2$@ICG-RGD was prepared. First, 5 mg of RGD was dissolved in 5 mL of 2-(N-morpholino) ethanesulfonic acid (MES) buffer (0.1 M, pH = 5.5). Then, 20 mg of N-(3-dimethylaminopropyl)-N′-ethylcarbodiimide hydrochloride (EDC) and 20 mg of N-hydroxysuccinimide (NHS) were added and gently stirred for 120 min at room temperature. Thereafter, 50 mg of HCeO$_2$@ICG was added into the above mixture and continuously stirred for 12 h. The as-prepared RGD anchored HCeO$_2$@ICG was washed by deionized water, followed by centrifugation at 5000 rpm for 10 min. The final product, HCeO$_2$@ICG-RGD, was dispersed in deionized water.

2.4. Cell Targeting and Intracellular ROS Generation Studies

The cellular uptake of HCeO$_2$@ICG-RGD and HCeO$_2$@ICG was observed by confocal laser scanning microscopy (CLSM). Briefly, 4T1 breast tumor cells were first seeded into 6-well plates with a cellular density of 1×10^5 per well and cultured for 24 h under 1 mL of 1640 medium (10% FBS, 100 units/mL of penicillin, and 100 μg/mL of streptomycin). After the treatment with HCeO$_2$@ICG-RGD and HCeO$_2$@ICG at a final concentration of 200 μg/mL for 12 h, respectively, all of the cell samples were washed with $1 \times$ PBS more than three times to stain the nuclei. Then, 1 μg/mL of DAPI was added into the above cells for 0.5 h. The as-prepared cell samples were observed under CLSM with 488 nm light excitation and an observation window from 550–600 nm.

The intracellular ROS generated evaluation of HCeO$_2$@ICG-RGD was observed by CLSM. Briefly, 1×10^5 per well of 4T1 cells were seeded into 6-well plates and cultured for 24 h under 1 mL of 1640 medium (10% FBS, 100 units/mL of penicillin, and 100 μg/mL of streptomycin). After the incubation with 200 μg/mL HCeO$_2$@ICG-RGD for 12 h, 808 nm laser was irradiated for 5 min (0.75 W cm^{-2}). Then, 4T1 cells co-incubated with PBS or HCeO$_2$@ICG-RGD were prepared following the same procedure. Furthermore, intracellular ROS production of all groups were estimated by DCHF-DA staining.

2.5. Fluorescent Imaging of Tumor Targeting and Photothermal Imaging In Vivo

All animal investigations were approved by the Medical Ethics Committee in South China University (USC202205XS02), which were performed in accordance with all relevant guidelines (Hengyang, China). Herein, 6-week-old female BALB/c nude mice were purchased from Shanghai SLAC Laboratory Animal Co., Ltd. (Shanghai, China). Subcutaneous tumor-bearing nude mice models were prepared by transcutaneous injection of tumor cells (1×10^6 4T1 cells dispersed in 150 μL PBS) into the right hindlimb muscle. When the tumor volume increased to ~200 mm^3, the ICG and $HCeO_2$@ICG-RGD were intravenously injected into tumor-bearing mice, respectively. Then, all the mice were imaged by the NIR fluorescent imaging system (NIR-OPTICS Series III 900/1700, 1000 nm long-pass filter) in a range of post-injection durations. Thereafter, major organs and tumors in the above two groups were collected after 24 h post-injection to obtain an ex vivo NIR II fluorescent image. Infrared region (IR) thermal imaging was employed for photothermal conversion in vivo. Tumor-bearing BALB/c nude mice received tail vein injection of 1X PBS and $HCeO_2$@ICG-RGD, respectively. The tumor site was irradiated with an 808 nm laser (1 W cm^{-2}) for 5 min at 24 h post-injection. After laser irradiation, in vivo IR thermal images were immediately obtained by a NIR thermal camera (FOTRIC 225s, Chinaprotech, Shanghai, China).

2.6. Synergistic Antitumor Studies of $HCeO_2$@ICG-RGD

To investigate antitumor ablation, tumor-bearing BALB/c nude mice were divided into five groups (n = 3) when the subcutaneous tumors reached a volume of ~150 mm^3. The animals had received various intravenous injections (PBS, $HCeO_2$+laser, $HCeO_2$-RGD+laser, $HCeO_2$@ICG+laser, and $HCeO_2$@ICG-RGD+laser) with the same $HCeO_2$ concentration at 8.2 mg/kg. Twenty-four hours after injection with the above formulations, nude mice in the last four groups were subjected to 5 min of NIR laser irradiation (808 nm, 1 W cm^{-2}). Tumor volume and body weight were recorded every 3 days. Importantly, tumors after the 9-day treatment were dissected and cut into tissue sections of 10 μm in thickness. Hematoxylin and eosin (H&E) and TdT-mediated dTUP-biotin nick end-labeling (TUNEL) staining studies were subsequently conducted. Meanwhile, after the 18-day treatment, the main organs (heart, liver, spleen, lung, and kidney) were also stained by H&E.

3. Results and Discussion

3.1. $HCeO_2$@ICG-RGD Fabrication

The synthesis of hollow mesoporous cerium oxide nanoparticles $HCeO_2$ and final ICG loading and RGD modification are shown in Figure 1. As depicted, $HCeO_2$ nanoenzymes were constructed by a hard-template strategy. Briefly, the template with ~100 nm of virus-like mesoporous silica ($VmSiO_2$) nanoparticles was first synthesized by a novel biphasic (water/cyclohexane) strategy with CTAB as the surfactant, TEOS as the silica precursor, and NaOH as the reductant. $VmSiO_2$ could be successfully synthesized after a 72-h reaction at the water–oil interface. Transmission electron microscope (TEM) was employed to observe the morphology of nanomaterials. As shown in Figure 2A, the as-made $VmSiO_2$ presented distinct nanotubes on the mesoporous surface with a uniform and monodispersed nanostructure. Then, ~21 nm of CeO_2 layer was in situ deposited on $VmSiO_2$ under methenamine solution with $Ce(NO_3)_3 \cdot 6H_2O$ as the CeO_2-based precursor (Figure 2B). Subsequently, the inner $VmSiO_2$ was removed under alkaline condition and the ~120 nm hollow cavity of CeO_2 was well maintained without collapse (Figure 2C). According to our previous reports, nanogranules of CeO_2 were reduced in situ, and then they assembled into a virus-like morphology [35,36]. The hollow CeO_2 nanoshells simulated the $VmSiO_2$ morphology, while the stacking mesopores of these CeO_2-based building blocks made them promising candidates for drug delivery. Furthermore, the stacking force in hollow metal oxide nanoparticles demonstrated vulnerability under acidic microenvironment (pH = 5.6). Then, the ICG was encapsulated into the hollow cavity and mesopores of this novel pH-sensitive $HCeO_2$ under room temperature ($HCeO_2$@ICG). The loading efficiency was calculated as 22.2%, proving the advantage of $HCeO_2$ for small therapeutics delivery. To facilitate the

following surface modification and prolong the blood circulation time, DSPE-PEG$_{2000}$-NH$_2$ molecules were coated onto the HCeO$_2$ surface. Finally, RGD was functionalized on HCeO$_2$ via EDC–NHS reaction (HCeO$_2$@ICG-RGD). As shown in Figure S1, the peak of 1423 cm^{-1} in Fourier transform infrared spectra (FTIR) was attributed to C–N from ICG, and then it disappeared, due to DSPE-PEG$_{2000}$-NH$_2$ modification. Interestingly, due to the formation of amide bond between HCeO$_2$@ICG-NH$_2$ and RGD, it clearly reappeared once again. Simultaneously, as displayed in X-ray diffraction (XRD) results, after ICG loading and RGD surface modification, a single broad diffused peak was still maintained in HCeO$_2$@ICG-RGD, suggesting that the nanogranules-packed HCeO$_2$ nanoenzymes are more susceptible to degradation (Figure S2). At the same time, we found that the specific surface area of HCeO$_2$@ICG-RGD decreased to 41.6% of the original HCeO$_2$, due to the cavity loading of ICG, and surface anchoring of both DSPE-PEG$_{2000}$-NH$_2$ and RGD (Figure S3). TEMs image of HCeO$_2$@ICG-RGD were obtained and the hollow nanostructure with rough surface was found, revealing that the morphology of HCeO$_2$ was not affected during ICG loading, NH$_2$ groups modification, and RGD anchoring (Figure 2D). To further confirm the rough surface, scanning electron microscope (SEM) was performed. Clearly, homogeneous nanotubes can be detected (Figure 2F). Undoubtedly, the nanotubes are capable of improving cell membrane adhesion, which fundamentally improves cellular internalization. Meanwhile, according to dark-field and high-angle annular dark field (HAADF) images, the cavity and rough surface could also be evidently detected (Figure 2F,G). In addition, the elemental mapping results presented that Ce and O were uniformly dispersed in the shell of HCeO$_2$@ICG-RGD. No other C element was found, further suggesting that after HCeO$_2$ was successfully obtained, it could be used as a CDT nanoagent.
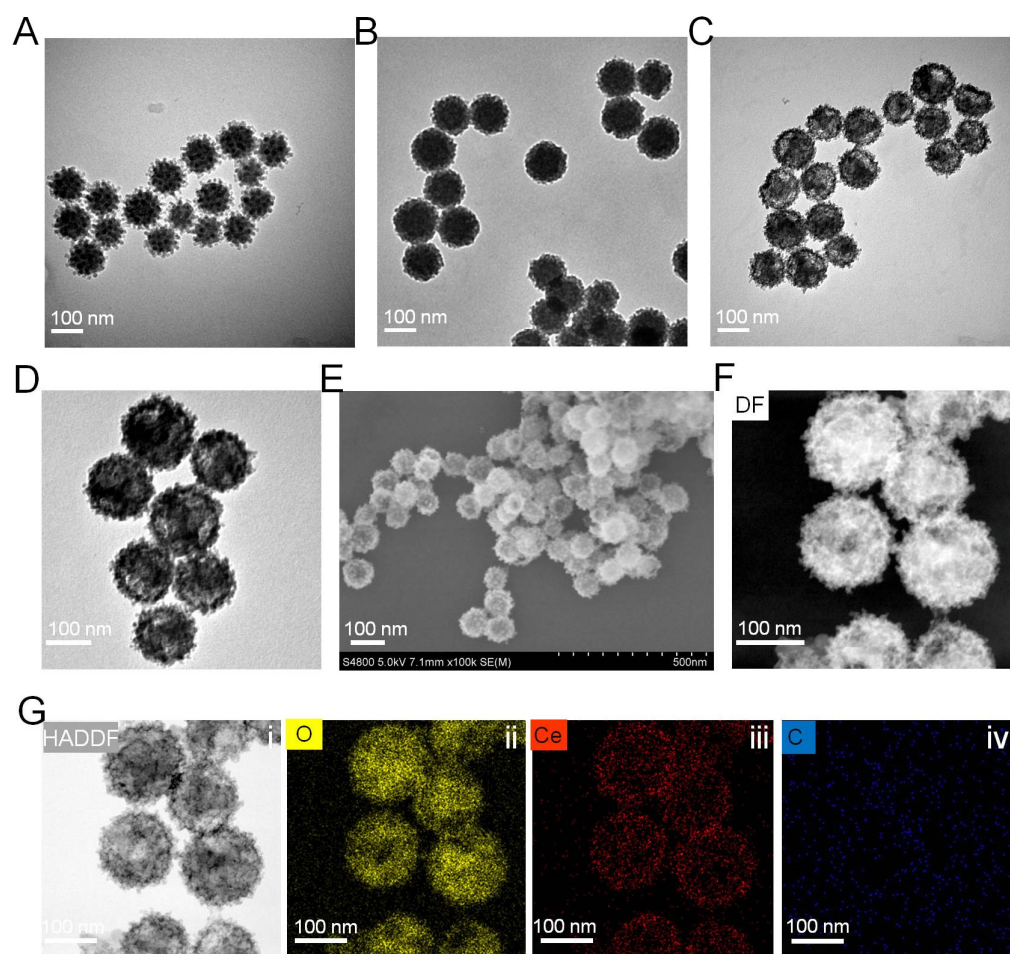

Figure 2. TEM images of virus-like mesoporous silica (**A**), CeO$_2$ coated mesoporous silica (**B**), HCeO$_2$

nanoparticles (**C**), and HCeO$_2$@ICG-RGD (**D**). SEM images of HCeO$_2$@ICG-RGD (**E**). Dark field (**F**), HADDF (**Gi**), O (**Gii**), Ce (**Giii**), C (**Giv**) elemental distribution images of HCeO$_2$@ICG-RGD.

3.2. HCeO$_2$@ICG-RGD Characterization

To further prove the ICG loading and RGD anchoring in HCeO$_2$, zeta-potential values of the above four kinds of nanoenzymes were also evaluated. As displayed in Figure 3A, the zeta potential of as-prepared HCeO$_2$@ICG decreased to −22.5 mV and it changed to positive charges after DSPE-PEG$_{2000}$-NH$_2$ coating. Finally, it slightly decreased after RGD functionalization (Figure 3A). All of the data suggested that ICG encapsulation in hollow cavity, NH$_2$ groups, and RGD molecules modification on the nanoenzyme surface have been successfully accomplished. Then, the average size of HCeO$_2$@ICG-RGD redispersed in different buffers was analyzed by dynamic light scattering (DLS). It exhibited values of ~120, 125, and 130 nm even after the 7-day incubation period in PBS, FBS, and serum, respectively, indicating the excellent size stability in biological fluids (Figure 3B). Accordingly, we subsequently studied the Ce ions and ICG release performance under acidic microenvironment. HCeO$_2$@ICG-RGD was treated with buffers under pH = 5.6 or pH = 7.4. Moreover, Ce ions in the residual HCeO$_2$@ICG-RGD were measured by ICP-OES. As shown in Figure 3C, they dramatically declined to 7.5% after 4 h of incubation. However, in pH = 7.4 treated solution, little Ce ions fluctuation was found and more than 90% of Ce was found in precipitation even at 4 h of co-culture. These data inspired us to investigate the morphology of HCeO$_2$@ICG-RGD under different pH values. Significantly, in pH = 5.6 buffer treated group, the CeO$_2$ shell became thinner after 1 h of incubation and almost all hollow nanostructures were destroyed after 2 h of treatment. Importantly, all HCeO$_2$ were completely collapsed and some CeO$_2$ nanogranules were observed. Nevertheless, in pH = 7.4 buffer incubated group, all intact HCeO$_2$ were discovered even after 4 h of co-culture (Figure 3D). In addition, TEM images indicated time-dependent decomposition performance of HCeO$_2$@ICG-RGD under acidic microenvironment. Moreover, the released ICG in the supernatant was recorded by UV-*vis* spectra. Almost more than 90% of ICG loading were detected after the pH = 5.6 buffer was treated for 4 h, which is consistent with the released Ce ions content at the same time point (Figure 3E). All results verified the ultrasensitive pH-sensitive degradation capability of HCeO$_2$@ICG-RGD, which could be applied for drug precise delivery and improved CDT efficiency, in comparison with the previously reported non-degradable CeO$_2$ nanoparticles [37–39]. Considering the strong absorption at near-infrared region (NIR) of ICG, the potential photothermal conversion behavior of HCeO$_2$@ICG was studied by 808 nm laser irradiation. As shown in Figure 3F,G, the temperature variation of HCeO$_2$@ICG displayed a time-dependent property. The results indicated that HCeO$_2$@ICG showed a superior photothermal generation performance with $\Delta T = 22$ °C increase after 5 min of irradiation by 808 nm NIR laser irradiation. While the temperature in the HCeO$_2$ group presented a slight increase ($\Delta T = 1$ °C) after 5 min of exposure. By comparison with HCeO$_2$@ICG, it demonstrated that ICG played a vital role in hyperthermia generation. Furthermore, all photothermal findings implied that HCeO$_2$@ICG could be utilized as an effective NIR photothermal agent.
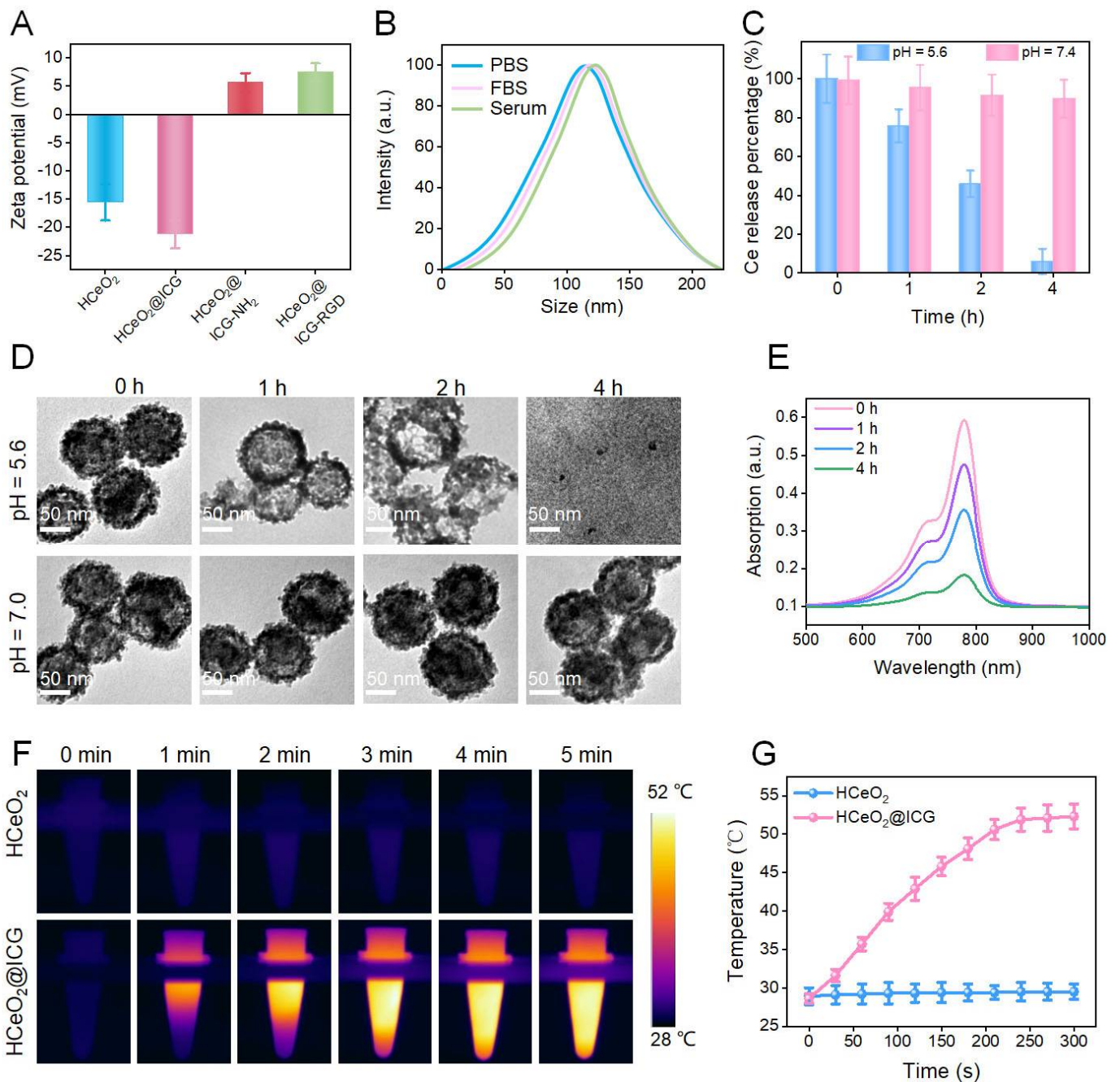
Figure 3. Zeta potential values of $HCeO_2$, $HCeO_2@ICG$, $HCeO_2@ICG-NH_2$, and $HCeO_2@ICG-RGD$ (**A**). Size distribution of $HCeO_2@ICG-RGD$ dispersed in PBS, FBS, and serum for 7 days (**B**). Ce ions release (**C**), TEM images (**D**) of $HCeO_2@ICG-RGD$ incubated in pH = 5.6 and 7.4 buffers for different times. (**E**)The released ICG fluorescence intensity of $HCeO_2@ICG-RGD$ incubated in pH = 5.6 for various durations. Infrared thermal images and (**F**) and temperature curve (**G**) of the solution containing $HCeO_2$ or $HCeO_2@ICG$ under the 808 nm laser (0.75 W cm^{-2}) irradiation for different minutes.

3.3. Cellular Uptake, ROS Generation, and Cell Killing Effect

Furthermore, the cell viability of breast tumor cells treated with HCeO$_2$@ICG−RGD was evaluated. At different experimental concentrations, HCeO$_2$@ICG−RGD had a negligible cytotoxicity toward normal cells (HUVEC) after 24 h of co-culture, and the cell viability still maintained a comparatively high (90%) viability (Figure S4). Interestingly, after incubation with 400 μg/mL of nanoenzymes for 24 h, only 75% of cells were alive (Figure 4A). The data suggested that our CeO$_2$-based nanoparticles exhibited excellent biocompatibility in normal cells and demonstrated notable cytotoxicity against tumor cells. This is primarily due to the CDT in CeO$_2$-based nanoagents. Subsequently, we studied the tumor cells targeting capability of this nanoenzyme. According to the CLSM images of 4T1 cells after treatment with HCeO$_2$@ICG-RGD or HCeO$_2$@ICG, the red fluorescence from ICG was higher in the HCeO$_2$@ICG-RGD group (Figure 4D). Meanwhile, as shown in Figure 4B, the quantitative fluorescent intensity was calculated, demonstrating that HCeO$_2$@ICG-RGD incubated tumor cells possessed significantly higher ICG in comparison with the non-RGD modified group. Various types of cell membrane receptors overexpressed in cancerous cells have been applied for receptor-mediated targeted delivery. One well-known receptor is $\alpha_v\beta_3$ integrin, which is highly overexpressed in the tumor-associated vasculature and several types of tumor cells, such as 4T1 murine breast cancer cells [40]. All of the above findings proved an efficient $\alpha_v\beta_3$ selectivity during breast tumor cell recognition in vivo. Intracellular ROS generation experiment was latterly conducted in cancerous cells. In PBS treatment, the green fluorescence was invisible, while strong fluorescence could be detected in HCeO$_2$@ICG-RGD groups, testifying the CDT effect of CeO$_2$-based nanoenzymes. Then, the influence of PTT on ROS production was monitored. Surprisingly, compared with the single CDT group with HCeO$_2$@ICG-RGD co-culture, we found that more dramatic green fluorescence was detected in the NIR laser irradiated group (Figure 4E). Accordingly, the mean fluorescent intensity of intracellular ROS was prominently higher than PBS and CDT groups (Figure 4C), further confirming that hyperthermia from PTT was beneficial for cytoplasm ROS generation. It has been demonstrated that sufficient hydroxyl radicals generation is capable of causing irreversible damage to organelles, especially for mitochondria, which can block protein transcription and reduce ATP levels that ultimately result in functional protein destruction. Meanwhile, Fenton-like reaction could further improve the tumor sensitivity toward hyperthermia. Therefore, the synergistic cell killing effect estimation was carried out by the CCK-8 kit assay in 4T1 cells under 808 nm laser irradiation. Clearly, in sharp contrast with single CDT with 75% live cells, only 38% cell viability was discovered in HCeO$_2$@ICG-RGD+laser group. Meanwhile, as shown in Figure 4F,G, the live/dead cells discrimination of synergistic PTT+CDT had the strongest tumor cell suppression ability in comparison with other formulations. Finally, the cell apoptosis ratio was conducted by Annexin V-FITC/PI assays after 12 h of treatment. Remarkably high apoptosis ratio was found in combination with the treated group (Figure 4H,I). In contrast, single CDT, PBS, and ICG+laser groups did not exhibit apoptotic tendency. Importantly, HCeO$_2$@ICG-RGD+laser displayed 45% cell apoptosis/necrosis after 24 h of incubation, which is in agreement with CCK-8 kit evaluation (Figure S5). Furthermore, all of the above cell killing investigations testified the overwhelming cell killing performance of PTT+CDT.
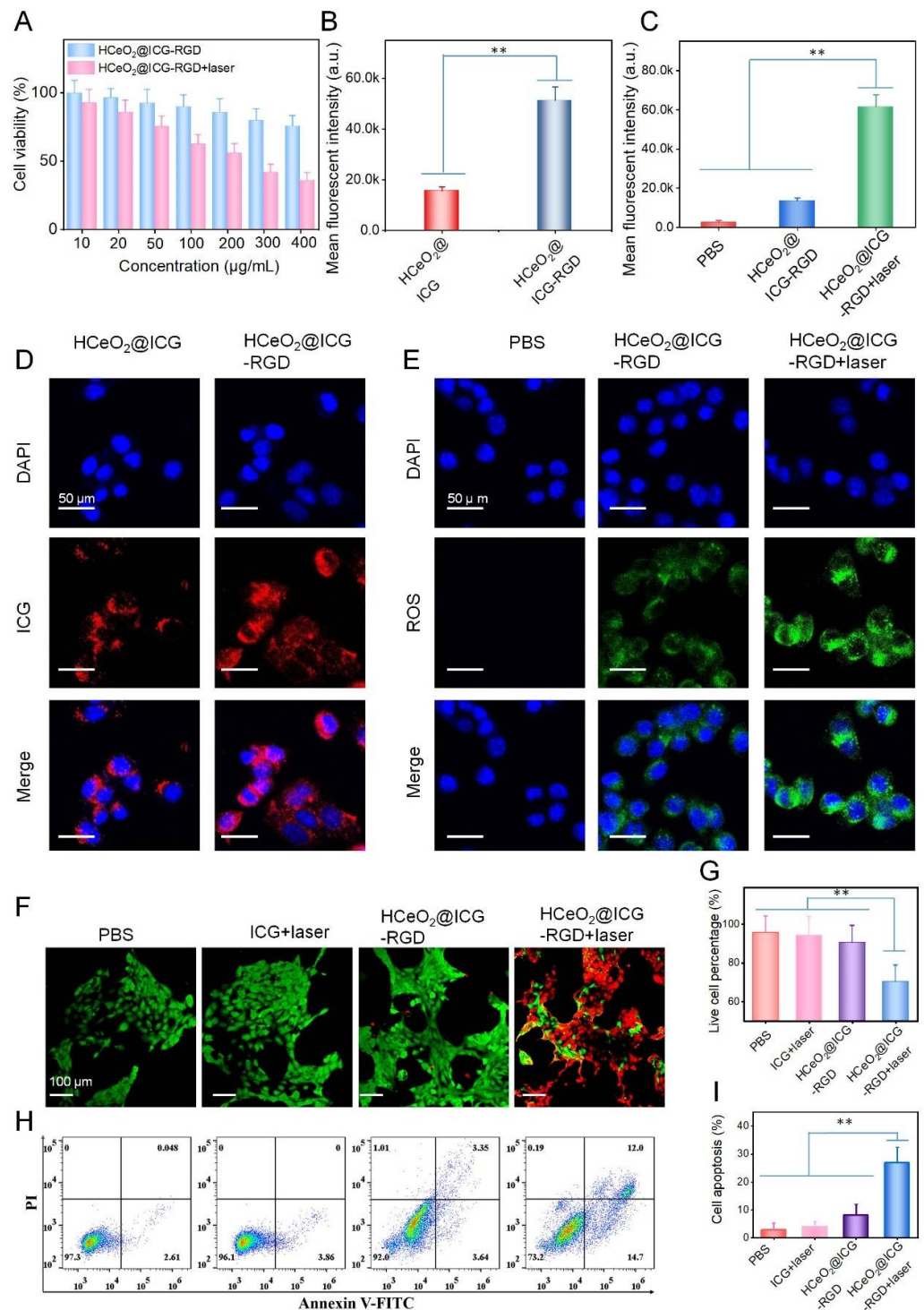
Figure 4. (**A**) Cell viability of 4T1 cells after 12 h of treatment with HCeO$_2$@ICG-RGD and HCeO$_2$@ICG-RGD+laser (808 nm, 0.75 W cm^{-2}, 5 min) at various concentrations. (**B,C**) Quantitative fluorescent intensity analysis of CLSM images in (**D,E**), respectively. (**D**) CLSM images of 4T1 cells after treatment with HCeO$_2$@ICG or HCeO$_2$@ICG-RGD for 12 h. (**E**) CLSM images of intracellular ROS generation after treatment with PBS, HCeO$_2$@ICG-RGD, and HCeO$_2$@ICG-RGD+laser for 12 h. Fluorescent images of live/dead cells (**F**) and flow cytometer analysis of cell apoptosis (**H**) after treatment with PBS, ICG+laser, HCeO$_2$@ICG-RGD, and HCeO$_2$@ICG-RGD+laser for 6 h. (**G,I**) Quantitative analysis of total live cells in (**F**) and cell apoptosis in (**H**), respectively. Mean $\pm$ SD for n = 4 (** $p < 0.01$ versus HCeO$_2$@ICG-RGD+laser, two-sided Student's *t*-test).

3.4. Tumor Targeting and Tumor Inhibition Capability In Vivo

After demonstrating the synergistic therapy function of HCeO$_2$@ICG-RGD in tumor cells, we would like to investigate this nanoenzyme in tumor model in vivo. First, we employed second near-infrared region (NIR II) fluorescence imaging (808 nm laser, 400 W cm^{-2}, 1000 nm long pass filter) in vivo to trace these nanoenzymes in subcutaneous 4T1 breast cancer bearing-mice after tail vein injection with HCeO$_2$@ICG-RGD (8.2 mg/kg) (Figure 5A). Meanwhile, no other NIR II fluorescence signals were observed in tumor site after free ICG injection. The ICG fluorescent signals in the tumor tissue of HCeO$_2$@ICG-RGD increased and reached a maximum level at 24 h post-injection, revealing the tumor accumulation capability of those HCeO$_2$@ICG-RGD nanoparticles. Meanwhile, ex vivo NIR II fluorescent images of major organs and tumors collected at 24 h post-injection were used for semi-quantitative biodistribution. As shown in Figure S6, the high tumor uptake of nanoenzymes was found in nanoenzyme group, and invisible signals were tracked in ICG group, further illustrating the tumor targeting performance of HCeO$_2$@ICG. Accordingly, PTT was performed at this peak accumulation time point. In vivo IR imaging results demonstrated that after irradiation by 808 nm laser for 5 min, the tumor tissue temperature of the control group mice was not notably increased and rapidly heated from 32 to 50 °C. Due to the enhanced permeability and retention (EPR) effect and RGD targeting modification that enhanced the affinity of HCeO$_2$@ICG-RGD toward tumor cells, a more efficient enrichment of nanoenzymes in the tumor tissue was observed, indicating that it could be used as an effective photothermal agent in vivo. Next, the tumor multi-mode therapy effect was further performed. As shown in Figure 5C,D, HCeO$_2$@ICG-RGD+laser had an excellent synergistic PTT+CDT antitumor ability with the tumor volume clearly reducing after 18 days of treatment. Moreover, the signal CDT administration (HCeO$_2$-RGD+laser) demonstrated some excellent tumor suppression capability. Furthermore, RGD modification can markedly improve the anticancer effect of tumor aggregation and augmentation. After 9 days of treatment, tumors were dissected for H&E and TUNEL staining analysis. No apparent apoptosis/necrosis was found in PBS group. Interestingly, HCeO$_2$-RGD+laser and HCeO$_2$@ICG+laser caused moderate apoptosis/necrosis by tumor targeting enhancement of single CDT and PTT after the EPR effect. Large areas of apoptosis/necrosis were detected in HCeO$_2$@ICG-RGD+laser group (808 nm laser 1 W cm^{-2}, 5 min) (Figure 5F). The synergistic PTT and CDT induced the most clear cell damage, especially apoptosis, which is also in accordance with tumor growth curves. Meanwhile, there were no apparent changes in body weight and pathological injury major organs, indicating the excellent biocompatibility of HCeO$_2$@ICG-RGD in vivo (Figures 5E and S7). Altogether, these data proved that our HCeO$_2$@ICG-RGD nanoplatform with excellent biosafety exhibited high potential for the clinical application of enhancing therapeutic efficacy via synergistic CDT/PTT.
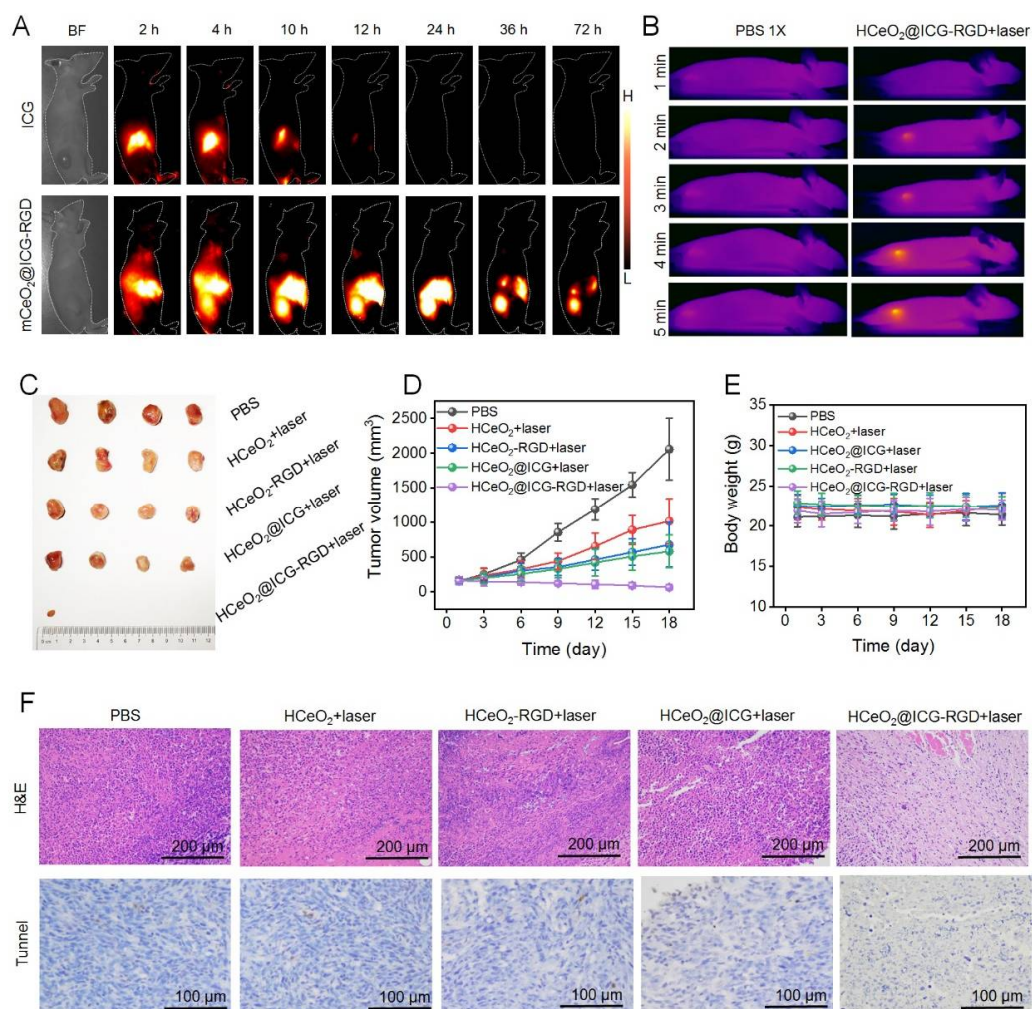
Figure 5. (**A**) NIR II fluorescent images of 4T1 breast tumor-bearing nude mice after tail vein administration of ICG or HCeO$_2$@ICG-RGD at various times. (**B**) IR thermal images of 4T1 breast tumor-bearing nude mice under 808 nm laser (1 W cm^{-2}) irradiation for different durations. Two groups of BALB/c nude mice were pretreated with tail vein administration of PBS or HCeO$_2$@ICG-RGD at 24 h. (**C**) Digital image of dissected solid breast tumors after 18 days of treatment with PBS, ICG+laser, HCeO$_2$-RGD+laser, HCeO$_2$@ICG+laser, and HCeO$_2$@ICG-RGD+laser. Tumor volume curves (**D**) and body weights measurement (**E**) of 4T1 breast tumor-bearing nude mice after PBS, ICG+laser, HCeO$_2$-RGD+laser, HCeO$_2$@ICG+laser, and HCeO$_2$@ICG-RGD+laser administration for different days. (**F**) H&E and TUNEL staining images of tumor tissues after 7 days of administration with PBS, ICG+laser, HCeO$_2$-RGD+laser, HCeO$_2$@ICG+laser, and HCeO$_2$@ICG-RGD+laser.

4. Conclusions

In conclusion, hollow mesoporous CeO$_2$-based nanoenzymes with ICG loading and RGD surface anchoring for synergistic CDT+PTT were successfully constructed using a hard-template strategy. The as-made HCeO$_2$@ICG-RGD demonstrated biodegradable behavior under acidic microenvironment in cytoplasm for ICG and Ce ions co-release. Then, massive ROS generation from CeO$_2$-based nanogranules was found under H$_2$O$_2$ triggering. The ICG release has an excellent photothermal conversion capability under 808 nm laser irradiation. Furthermore, PTT could effectively assist CDT due to the rise in hyperthermia, and, in turn, CDT made tumor cells more susceptible toward PTT. In vivo results exhibited that our nanoenzymes had excellent tumor targeting capability via active selectivity and EPR effect. More importantly, mutually reinforcing CDT and PTT can effectively eradicate the malignant solid breast tumors without systematic toxicity. This

work paved a fascinating way to obtain self-reinforced PTT+CDT with high specificity based on CeO_2-based nanoplatform, which will have a potential value in cancerous therapy.

Although $HCeO_2$@ICG-RGD demonstrated a small amount of off-targeted side effect during the tumor eradication period, the considerations regarding the long-term biosafety should still be seriously considered. Further studies on the biocompatibility and biodistribution of our CeO_2-based nanoenzymes and their biodegradation byproducts should also be conducted. Owing to the main obstacle of the preclinical translation of nanoparticles is the uncontrollable fate and systematic harmfulness in vivo. Once inoculated, it remains difficult to follow the trail of the fate of nanoparticles in vivo. Additionally, this can allow the targeted tumor site to reach other major organs, where they can extensively accumulate and be toxic. Therefore, investigations on how to fabricate safer CeO_2-based nanoenzymes in vivo, through functionalized or modification strategies, are very crucial.

Supplementary Materials: The following supporting information can be downloaded at: https://www.mdpi.com/article/10.3390/pharmaceutics14081717/s1. Figure S1: Nitrogen adsorption–desorption isotherms of $HCeO_2$ (A) and $HCeO_2$@ICG-RGD (B). Figure S2: FTIR spectra of $HCeO_2$, $HCeO_2$@ICG, $HCeO_2$@ICG-NH_2, and $HCeO_2$@ICG-RGD. Figure S3: XRD spectra of $HCeO_2$, $HCeO_2$@ICG, $HCeO_2$@ICG-NH_2, and $HCeO_2$@ICG-RGD. Figure S4: Cell viability of normal cells (HUVEC) after 24 h of treatment with $HCeO_2$@ICG-RGD. Figure S5: Cell apoptosis analyzation of PBS- and $HCeO_2$@ICG-RGD+laser-treated 4T1 cells via Annexin-V FITC and PI staining. Figure S6: Ex vivo bright field image (left) and NIR II fluorescent image of major organs (heart, liver, spleen, lung, kidney) and tumors after tail vein injection of $HCeO_2$@ICG-RGD at 24 h. Figure S7: H&E staining images of major organs (heart, liver, spleen, lung, kidney) from breast tumor-bearing mice after different treatments (PBS, $HCeO_2$+laser, $HCeO_2$@ICG+laser, $HCeO_2$@ICG+laser, and $HCeO_2$@ICG-RGD+laser) for 18 days.

Author Contributions: Conceptualization, H.T., Q.C. and L.H.; methodology, Y.L. and J.M.; validation, P.W.; investigation, H.T., L.H. and Q.C.; data curation, P.W.; writing—original draft preparation, P.W.; writing—review and editing, L.H. and P.W.; supervision, L.H.; funding acquisition, H.T. All authors have read and agreed to the published version of the manuscript.

Institutional Review Board Statement: The animal study protocol was approved by the Medical Ethics Committee, University of South China (protocol code USC202205XS02 and 10 May 2022).

Informed Consent Statement: Not applicable.

Data Availability Statement: Not applicable.

Conflicts of Interest: The authors declare no conflict of interest.

References

1. Srinivas, U.S.; Tan, B.W.Q.; Vellayappan, B.A.; Jeyasekharan, A.D. ROS and the DNA damage response in cancer. *Redox Biol.* **2019**, *25*, 101084. [CrossRef] [PubMed]
2. Tuy, K.; Rickenbacker, L.; Hjelmeland, A.B. Reactive oxygen species produced by altered tumor metabolism impacts cancer stem cell maintenance. *Redox Biol.* **2021**, *44*, 101953. [CrossRef] [PubMed]
3. Trachootham, D.; Alexandre, J.; Huang, P. Targeting Cancer cells by ROS-mediated mechanisms: A radical therapeutic approach. *Nat. Rev. Drug Discov.* **2009**, *8*, 579–591. [CrossRef] [PubMed]
4. Zhu, Y.; Yu, F.; Tan, Y.; Wen, L.; Li, Y.; Yuan, H.; Hu, F. Guiding appropriate timing of laser irradiation by polymeric micelles for maximizing chemo-photodynamic therapy. *Int. J. Nanomed.* **2020**, *15*, 6531–6543. [CrossRef]
5. An, J.; Hu, Y.G.; Cheng, K.; Li, C.; Hou, X.L.; Wang, G.L.; Zhang, X.S.; Liu, B.; Zhao, Y.D.; Zhang, M.Z. ROS-augmented and tumor-microenvironment responsive biodegradable nanoplatform for enhancing chemo-sonodynamic therapy. *Biomaterials* **2020**, *234*, 119761. [CrossRef]
6. Siddique, S.; Chow, J.C.L. Application of nanomaterials in biomedical imaging and cancer therapy. *Nanomaterials* **2020**, *10*, 1700. [CrossRef]
7. Tang, X.L.; Wang, Z.; Zhu, Y.Y.; Xiao, H.; Xiao, Y.; Cui, S.; Lin, B.L.; Yang, K.; Liu, H.Y. Hypoxia-activated ROS burst liposomes boosted by local mild hyperthermia for photo/chemodynamic therapy. *J. Control. Release* **2020**, *328*, 100–111. [CrossRef]

8. Zhang, L.; Li, C.X.; Wan, S.S.; Zhang, X.Z. Nanocatalyst-mediated chemodynamic tumor therapy. *Adv. Healthc. Mater.* **2022**, *11*, e2101971. [CrossRef]

9. Tang, Z.; Liu, Y.; He, M.; Bu, W. Chemodynamic therapy: Tumour microenvironment-mediated Fenton and Fenton-like reactions. *Angew. Chem. Int. Ed.* **2019**, *58*, 946–956. [CrossRef]

10. Yu, Z.; Lou, R.; Pan, W.; Li, N.; Tang, B. Nanoenzymes in disease diagnosis and therapy. *Chem. Commun.* **2020**, *56*, 15513–15524. [CrossRef]

11. Zhu, P.; Chen, Y.; Shi, J. Nanoenzyme-augmented cancer sonodynamic therapy by catalytic tumor oxygenation. *ACS Nano* **2018**, *12*, 3780–3795. [CrossRef] [PubMed]

12. Yao, H.; Guo, X.; Zhou, H.; Ren, J.; Li, Y.; Duan, S.; Gong, X.; Du, B. Mild Acid-responsive "nanoenzyme capsule" remodeling of the tumor microenvironment to increase tumor penetration. *ACS Appl. Mater. Interfaces* **2020**, *12*, 20214–20227. [CrossRef] [PubMed]

13. Xu, K.; Wu, X.; Cheng, Y.; Yan, J.; Feng, Y.; Chen, R.; Zheng, R.; Li, X.; Song, P.; Wang, Y.; et al. A biomimetic nanoenzyme for starvation therapy enhanced photothermal and chemodynamic tumor therapy. *Nanoscale* **2020**, *12*, 23159–23165. [CrossRef]

14. Li, Y.; Zhou, J.; Wang, L.; Xie, Z. Endogenous hydrogen sulfide-triggered MOF-based nanoenzyme for synergic cancer therapy. *ACS Appl. Mater. Interfaces* **2020**, *12*, 30213–30220. [CrossRef]

15. Wang, S.; Zhao, J.; Zhang, L.; Zhang, C.; Qiu, Z.; Zhao, S.; Huang, Y.; Liang, H. A unique multifunctional nanoenzyme tailored for triggering tumor microenvironment activated NIR-II photoacoustic imaging and chemodynamic/photothermal combined therapy. *Adv. Healthc. Mater.* **2022**, *11*, e2102073. [CrossRef] [PubMed]

16. Wang, D.; Wu, H.; Lim, W.Q.; Phua, S.; Xu, P.; Chen, Q.; Guo, Z.; Zhao, Y. A Mesoporous nanoenzyme derived from metal-organic frameworks with endogenous oxygen generation to alleviate tumor hypoxia for significantly enhanced photodynamic therapy. *Adv. Mater.* **2019**, *31*, e1901893. [CrossRef]

17. Li, J.; Xie, C.; Huang, J.; Jiang, Y.; Miao, Q.; Pu, K. Semiconducting Polymer Nanoenzymes with Photothermic Activity for Enhanced Cancer Therapy. *Angew. Chem. Int. Ed.* **2018**, *57*, 3995–3998. [CrossRef]

18. Zeng, L.; Cheng, H.; Dai, Y.; Su, Z.; Wang, C.; Lei, L.; Lin, D.; Li, X.; Chen, H.; Fan, K.; et al. In vivo regenerable cerium oxide nanozyme-loaded pH/H_2O_2-responsive nanovesicle for tumor-targeted photothermal and photodynamic therapies. *ACS Appl. Mater. Interfaces* **2021**, *13*, 233–244. [CrossRef]

19. Fan, Y.; Li, P.; Hu, B.; Liu, T.; Tang, Y. A Smart photosensitizer-cerium oxide nanoprobe for highly selective and efficient photodynamic therapy. *Inorg. Chem.* **2019**, *58*, 7295–7302. [CrossRef]

20. Wang, Y.; Shen, X.; Chen, F. Improving the catalytic activity of CeO_2/H_2O_2 system by sulfation pretreatment of CeO_2. *J. Mol. Catal. A Chem.* **2013**, *381*, 38–45. [CrossRef]

21. Fu, L.H.; Wan, Y.; Qi, C.; He, J.; Li, C.; Yang, C.; Xu, H.; Lin, J.; Huang, P. Nanocatalytic theranostics with glutathione depletion and enhanced reactive oxygen species generation for efficient cancer therapy. *Adv. Mater.* **2021**, *33*, e2006892. [CrossRef] [PubMed]

22. Ma, Y.; Xu, H.; Sun, B.; Du, S.; Cui, S.; Zhang, L.; Ding, N.; Yang, D. pH-responsive oxygen and hydrogen peroxide self-supplying nanosystem for photodynamic and chemodynamic therapy of wound infection. *ACS Appl. Mater. Interfaces* **2021**, *13*, 59720–59730. [CrossRef] [PubMed]

23. Liu, Z.; Li, T.; Han, F.; Wang, Y.; Gan, Y.; Shi, J.; Wang, T.; Akhtar, M.L.; Li, Y. A cascade-reaction enabled synergistic cancer starvation/ROS-mediated/chemo-therapy with an enzyme modified Fe-based MOF. *Biomater. Sci.* **2019**, *7*, 3683–3692. [CrossRef] [PubMed]

24. Chen, Y.; Yin, C.; Zhang, Y.; Liu, Y.; Huang, W. "Dual lock-and-key"-controlled ceria nanotubes-based nanozymes for tumor-specific photothermal therapy. *Dyes Pigment.* **2021**, *191*, 109350. [CrossRef]

25. Zheng, X.; Xing, D.; Zhou, F.; Wu, B.; Chen, W.R. Indocyanine green-containing nanostructure as near infrared dual-functional targeting probes for optical imaging and photothermal therapy. *Mol. Pharm.* **2011**, *8*, 447–456. [CrossRef]

26. Wang, Z.; Fu, L.; Zhu, Y.; Wang, S.; Shen, G.; Jin, L.; Liang, R. Chemodynamic/photothermal synergistic therapy based on Ce-doped Cu-Al layered double hydroxides. *J. Mater. Chem. B* **2021**, *9*, 710–718. [CrossRef]

27. Yoon, H.; Lee, H.; Lim, J.; Park, J. Liposomal indocyanine green for enhanced photothermal therapy. *ACS Appl. Mater. Interfaces* **2017**, *9*, 5683–5691. [CrossRef]

28. Li, X.; Wei, Z.; Bie, N.; Zhang, X.; Zhan, G.; Li, J.; Qin, J.; Yu, J.; Zhang, B.; Gan, L.; et al. Reversing insufficient photothermal therapy-induced tumor relapse and metastasis by regulating cancer-associated fibroblasts. *Nat. Commun.* **2022**, *13*, 2794. [CrossRef]

29. Chen, Q.; Luo, Y.; Du, W.; Liu, Z.; Zhang, S.; Yang, J.; Yao, H.; Liu, T.; Ma, M.; Chen, H. Clearable theranostic platform with a pH-independent chemodynamic therapy enhancement strategy for synergetic photothermal tumor therapy. *ACS Appl. Mater. Interfaces* **2019**, *11*, 18133–18144. [CrossRef]

30. Huo, M.; Wang, L.; Wang, Y.; Chen, Y.; Shi, J. Nanocatalytic tumor therapy by single-atom catalysts. *ACS Nano* **2019**, *13*, 2643–2653. [CrossRef]

31. Nie, X.; Xia, L.; Wang, H.L.; Chen, G.; Wu, B.; Zeng, T.Y.; Hong, C.Y.; Wang, L.H.; You, Y.Z. Photothermal therapy nanomaterials boosting transformation of Fe(III) into Fe(II) in tumor cells for highly improving chemodynamic therapy. *ACS Appl. Mater. Interfaces* **2019**, *11*, 31735–31742. [CrossRef] [PubMed]

32. Chen, W.H.; Luo, G.F.; Lei, Q.; Hong, S.; Qiu, W.X.; Liu, L.H.; Cheng, S.X.; Zhang, X.Z. Overcoming the heat endurance of tumor cells by interfering with the anaerobic glycolysis metabolism for improved photothermal therapy. *ACS Nano* **2017**, *11*, 1419–1431. [CrossRef]

33. Sheng, D.; Liu, T.; Deng, L.; Zhang, L.; Li, X.; Xu, J.; Hao, L.; Li, P.; Ran, H.; Chen, H.; et al. Perfluorooctyl bromide & indocyanine green co-loaded nanoliposomes for enhanced multimodal imaging-guided phototherapy. *Biomaterials* **2018**, *165*, 1–13.

34. Wang, W.; Wang, P.; Tang, X.; Elzatahry, A.A.; Wang, S.; Dahyan, D.A.; Zhao, M.; Yao, C.; Hung, C.; Zhu, X.; et al. Facile synthesis of uniform virus-like mesoporous silica nanoparticles for enhanced cellular internalization. *ACS Cent. Sci.* **2017**, *3*, 839–846. [CrossRef]

35. Yang, R.; Wang, P.; Lou, K.; Dang, Y.; Tian, H.; Li, Y.; Gao, Y.; Huang, W.; Zhang, Y.; Liu, X.; et al. Biodegradable nanoprobe for NIR-II fluorescence image-guided surgery and enhanced breast cancer radiotherapy efficacy. *Adv. Sci.* **2022**, *9*, 2104728. [CrossRef]

36. Liu, Z.; Wang, P.; Xie, F.; Chen, J.; Cai, M.; Li, Y.; Yan, J.; Lin, Q.; Luo, F. Virus-inspired hollow mesoporous gadolinium-bismuth nanotheranostics for magnetic resonance imaging-guided synergistic photodynamic-radiotherapy. *Adv. Healthc. Mater.* **2022**, *11*, 2102060. [CrossRef]

37. Shao, C.; Shen, A.; Zhang, M.; Meng, X.; Song, C.; Liu, Y.; Gao, X.; Wang, P.; Bu, W. Oxygen vacancies enhanced CeO_2:Gd nanoparticles for sensing a tumor vascular microenvironment by magnetic resonance imaging. *ACS Nano* **2018**, *12*, 12629–12637. [CrossRef] [PubMed]

38. Tapeinos, C.; Battaglini, M.; Prato, M.; Rosa, G.L.; Scarpellini, A.; Ciofani, G. CeO_2 Nanoparticles-loaded pH-responsive microparticles with antitumoral properties as therapeutic modulators for osteosarcoma. *ACS Omega* **2018**, *3*, 8952–8962. [CrossRef] [PubMed]

39. Pugachevskii, M.; Kim, E.S.; Kim, N.Y. Selectively acting agent based on ablated CeO_2 nanoparticles for photodynamic therapy of brain cancer. *BRO Rep.* **2019**, *6*, S54–S345. [CrossRef]

40. Li, H.; Wang, M.; Huang, B.; Zhu, S.W.; Zhou, J.J.; Chen, D.R.; Cui, R.; Zhang, M.; Sun, Z.J. Theranostic near-infrared-IIb emitting nanoprobes for promoting immunogenic radiotherapy and abscopal effects against cancer metastasis. *Nat. Commun.* **2021**, *12*, 7149. [CrossRef]